

Cite this: DOI: 00.0000/xxxxxxxxxx

Rheology of active polar emulsions: from linear to unidirectional and unviscid flow, and intermittent viscosity[†]

G. Negro^{*a}, L.N. Carenza^{*a}, A. Lamura^b, A. Tiribocchi^{*c} and G. Gonnella^{a‡}

Received Date

Accepted Date

DOI: 00.0000/xxxxxxxxxx

The rheological behaviour of an emulsion made of an active polar component and an isotropic passive fluid is studied by lattice Boltzmann methods. Different flow regimes are found by varying the values of shear rate and extensile activity (occurring, e.g., in microtubule-motor suspensions). By increasing activity, a first transition occurs from linear flow regime to spontaneous persistent unidirectional macro-scale flow, followed by another transition either to (low shear) intermittent flow regime with coexistence of states with positive, negative, and vanishing apparent viscosity, or to (high shear) symmetric shear thinning regime. The different behaviours can be explained in terms of the dynamics of the polarization field close to the walls. A maximum entropy production principle selects the most likely states in the intermittent regime.

1 Introduction

Active gels^{1–3} are a new class of complex fluids with striking physical properties and many possible innovative applications^{4–8}. As other kinds of active systems^{9–17}, they are maintained in their driven state – far from thermodynamic equilibrium – by energy supplied directly and independently at the level of individual constituents. Examples are suspensions of biological filaments, such as actomyosin and microtubule bundles, activated with motor proteins^{18–21} and bacterial cultures^{22,23}. The constituents of these systems have the natural tendency to assemble and align, thus developing structures with typical polar or nematic order. Combination of this property with self-motility capacity is at the origin of a wealth of interesting phenomena, not observable in absence of activity²⁴, including spontaneous flow^{1,25,26}, active turbulence at low Reynolds numbers^{22,27,28}, and unusual rheological properties^{3,29}. Most of these behaviours were found in single component fluids, while mixtures of active and passive components have not been too much investigated so far³⁰.

Complex rheological behaviours in active matter depend on the interplay between the external forcing and the circulating flow induced by active agents. For instance, the swimming mechanism of pusher microswimmers, like *E. Coli*, produces a far flow field characterized by quadrupolar symmetry, in which fluid is expelled along the fore-aft axes of the swimmer and drawn transversely,

thus leading to *extensile* flow patterns. These enforce the applied flow, in the case of flow-aligning swimmers, causing shear thinning³¹. This may lead to the occurrence of a *superfluidic* regime with vanishing (apparent) shear viscosity that was speculated in³² for the case of an active liquid crystals close to the isotropic-nematic transition. Experiments^{33,34} and further theories³⁵ confirmed that extensile active components are able to lower the viscosity of thin film suspensions. An effective inviscid flow was observed in³⁶ and more recently in³⁷, when the concentration and activity of *E. Coli* are sufficiently large to support coherent collective swimming. A related feature in extensile gels is the appearance of persistent uni-directional flows in experiments on bacterial suspensions³⁸ and ATP-driven gels³⁹. Recently, numerical simulations in quasi-1d geometries and linear analysis of active polar liquid crystal models have shown the occurrence of vanishing and even negative viscosity states⁴⁰. However, a complete characterization of the rheology of fully 2d active compounds has never been accomplished so far, despite being fundamental to unveil dynamical mechanisms leading to the complex properties presented. We also mention that puller swimmers – exerting a contractile force dipole on the surrounding fluid – still generate a quadrupolar far flow field, but this time the fluid is expelled transversely to its body. This explains the shear thickening behaviour, observed in experiments performed on suspensions of *C. reinhardtii*⁴¹ – a species of micro-alga that propels itself by means of two flagella producing contractile movements – and in numerical studies on contractile gels^{26,35,42}. In this paper we will focus on extensile systems.

We study, by extensive lattice Boltzmann simulations, the rheology of a 2d emulsion, made of an active fluid component (a polar gel) and an isotropic passive fluid, under simple shear flows.

^{0a} Dipartimento di Fisica, Università degli Studi di Bari and INFN, Sezione di Bari, via Amendola 173, Bari, I-70126, Italy

^{0b} Istituto Applicazioni Calcolo, CNR, Via Amendola 122/D, I-70126 Bari, Italy

^{0c} Center for Life Nano Science@La Sapienza, Istituto Italiano di Tecnologia, 00161 Rome, Italy and Istituto per le Applicazioni del Calcolo CNR, via dei Taurini 19, 00185 Rome, Italy

The system that we consider^{43,44} has the property that a tunable amount of active material can be homogeneously dispersed in an emulsion. With respect to the single-component active gel theory, this approach has the great advantage that the typical length-scale of active injection can be kept under control by setting opportunely the parameters of the model. This would also delucidate the mechanisms for the rich rheological behaviour previously described. Experimental realization can be achieved by either confining activated cellular extracts in an emulsion of water-in-oil^{20,21} or dispersing bacteria in water, ensuring microphase separation through depletion forces and a suitable surfactant⁴⁵.

In Sect. 2 we describe the model for active emulsions and the lattice Boltzmann method implemented for the numerical study. Moreover, we introduce our main adimensional parameters that are related to the strength of both active injection and shear flow. In Sect. 3 we describe the numerical results for the flow behaviour in a region of the parameter space characterized by a double transition, first from linear velocity profiles to unidirected motion and then, by increasing activity, to symmetric shear thinning behaviour. We describe the relevance of the role of the polarization and active stress in proximity of external walls. In Sect. 4 intermittent flow – occurring in a region of the parameter space at low shear rate and sufficiently high viscosity – will be analyzed, also in terms of the entropy production rate evaluated for the different coexisting flow states. Finally, in Sect. 5 we show the phase diagram summarizing results for the different behaviours we have found and we draw some conclusions.

2 Model and Numerical Methods

We outline here the hydrodynamic model and the numerical method used to conduct our study. We consider a fluid in 2d comprising a mixture of active material and an isotropic solvent with total mass density ρ . The physics of the resulting composite material can be described by using an extended version of the well-established active gel theory^{1,3,24,46–48}. The hydrodynamic variables are the density of the fluid ρ , its velocity \mathbf{v} , the concentration of the active material ϕ , and the polarization \mathbf{P} , which accounts for the average orientation of the active constituents. The dynamical equations ruling the evolution of the system in the incompressible limit are:

$$\rho \left(\frac{\partial}{\partial t} + \mathbf{v} \cdot \nabla \right) \mathbf{v} = \nabla \cdot \tilde{\sigma}^{tot}, \quad (1)$$

$$\frac{\partial \phi}{\partial t} + \nabla \cdot (\phi \mathbf{v}) = M \nabla^2 \mu, \quad (2)$$

$$\frac{\partial \mathbf{P}}{\partial t} + (\mathbf{v} \cdot \nabla) \mathbf{P} = -\tilde{\Omega} \cdot \mathbf{P} + \xi \tilde{D} \cdot \mathbf{P} - \frac{1}{\Gamma} \mathbf{h}. \quad (3)$$

The first one is the Navier-Stokes equation, where $\tilde{\sigma}^{tot}$ is the total stress tensor⁴⁹. Eqs. (2)-(3) govern the time evolution of the concentration of the active material and of the polarization field, respectively. By the assumption that the amount of the active component is locally conserved, the evolution of the concentration field, Eq. (2), can be written as a convection-diffusion equation, where M is the mobility, $\mu = \delta F / \delta \phi$ the chemical potential, with F a suitable free energy functional, encoding the equilib-

rium properties of the system, to be defined later. The dynamics of the polarization field follows an advection-relaxation equation, Eq. (3), borrowed from polar liquid crystal theory. Here Γ is the rotational viscosity, ξ is a constant controlling the aspect ratio of active particles (positive for rod-like particles and negative for disk-like ones) and their response to external flows ($|\xi| > 1$ for flow-aligning particles and $|\xi| < 1$ for flow-tumbling ones), while $\mathbf{h} = \delta F / \delta \mathbf{P}$ is the molecular field. $\tilde{D} = (\tilde{W} + \tilde{W}^T)/2$ and $\tilde{\Omega} = (\tilde{W} - \tilde{W}^T)/2$ respectively represent the symmetric and the anti-symmetric parts of the velocity gradient tensor $W_{\alpha\beta} = \partial_\beta v_\alpha$, where Greek indexes denote Cartesian components. These contributions are in addition to the material derivative, as the liquid crystal can be rotated or aligned by the fluid⁴⁹.

The stress tensor $\tilde{\sigma}^{tot}$ considered in the Navier-Stokes equation, Eq. (1), can be splitted into an equilibrium/passive and a non-equilibrium/active part:

$$\tilde{\sigma}^{tot} = \tilde{\sigma}^{pass} + \tilde{\sigma}^{act}. \quad (4)$$

The passive term accounts for the viscous dissipation and reactive phenomena – the elastic response of the binary fluid and of the liquid crystal – and is given by four contributions:

$$\tilde{\sigma}^{pass} = \tilde{\sigma}^{hydro} + \tilde{\sigma}^{visc} + \tilde{\sigma}^{pol} + \tilde{\sigma}^{bm}. \quad (5)$$

The first term is the hydrodynamic pressure contribution given by $\sigma_{\alpha\beta}^{hydro} = -p \delta_{\alpha\beta}$. The second term is the viscous stress, written as $\sigma_{\alpha\beta}^{visc} = \eta_0 (\partial_\alpha v_\beta + \partial_\beta v_\alpha)$, where η_0 is the shear viscosity. The second term is the polar elastic stress, analogous to the one used in nematic liquid crystal hydrodynamics⁴⁹:

$$\sigma_{\alpha\beta}^{pol} = \frac{1}{2} (P_\alpha h_\beta - P_\beta h_\alpha) - \frac{\xi}{2} (P_\alpha h_\beta + P_\beta h_\alpha) - k_P \partial_\alpha P_\gamma \partial_\beta P_\gamma, \quad (6)$$

where k_P is the elastic constant of the liquid crystal, in the single constant approximation⁵⁰. The third term on the right-hand side of Eq. (5) is borrowed from binary mixture theories and it includes interfacial contribution between the two phases:

$$\sigma_{\alpha\beta}^{bm} = \left(f - \phi \frac{\delta F}{\delta \phi} \right) \delta_{\alpha\beta} - \frac{\delta F}{\partial (\partial_\beta \phi)} \partial_\alpha \phi, \quad (7)$$

where we have denoted with f the free energy density. The active contribution to the stress tensor, the only one not stemming from the free energy, is given by^{25,48}

$$\sigma_{\alpha\beta}^{act} = -\zeta \phi \left(P_\alpha P_\beta - \frac{1}{3} |\mathbf{P}|^2 \delta_{\alpha\beta} \right), \quad (8)$$

where ζ is the activity strength, positive for extensile systems (pushers) and negative for contractile ones (pullers). The active stress drives the system out of equilibrium, by injecting energy on the typical lengthscales of deformation of the polarization pattern.

By assuming that local equilibrium is satisfied even in presence of activity, the thermodynamics forces in Eq. (1)-(3) can be deduced by the following free-energy functional, coupling the Landau-Brazovskii model^{51,52} to the distortion free-energy of a

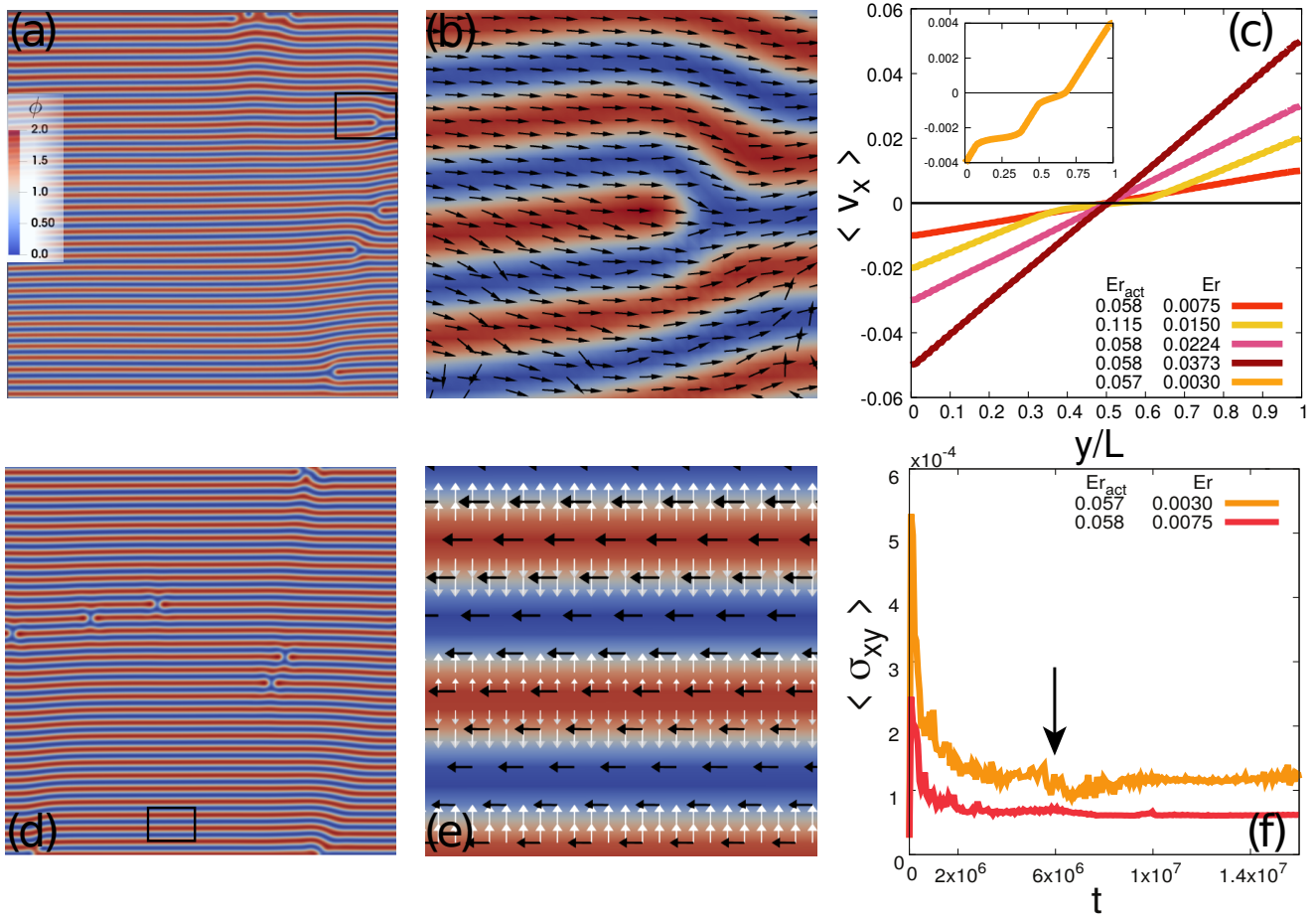


Fig. 1 Linear velocity profiles and lamellar phase. Concentration contour plots at $Er_{act} = 0.057$, $Er = 0.0030$ and $Er_{act} = 0.058$, $Er = 0.0075$ are respectively shown in panels (a) and (d). Here (and in the rest of the paper) red regions correspond to the active phase ($\phi \approx 2.0$), while blue regions to the passive fluid ($\phi \approx 0.0$). Panels (b) and (e) show a zoom of the regions highlighted by the black squares in panel (a) and (d). Black and white vectors respectively denote velocity and polarization fields in panel (e), while only the velocity field has been plotted in panel (b). Panels (c) and (f) show the averaged velocity profile and the time evolution of the shear stress (red and orange curves correspond to the cases considered in panel (a) and (d)). Black arrow in panel (f) points to a jump in the relaxation of σ_{xy} , due to the annihilation of two dislocations. Note that in the present Figure, as well as in the followings, the colors of the velocity and the stress profiles have been chosen in relation to the colors of the corresponding region of the phase diagram of Fig. 8. In panels (c-f) the profiles have been plotted in such a way to make reference to the red/orange region of linear profiles.

polar system:

$$F[\phi, \mathbf{P}] = \int d\mathbf{r} \left\{ \frac{\tilde{a}}{4\phi_{cr}^2} \phi^2 (\phi - \phi_0)^2 + \frac{k_\phi}{2} |\nabla \phi|^2 + \frac{c}{2} (\nabla^2 \phi)^2 - \frac{\alpha}{2} \frac{(\phi - \phi_{cr})}{\phi_{cr}} |\mathbf{P}|^2 + \frac{\alpha}{4} |\mathbf{P}|^4 + \frac{k_p}{2} (\nabla \mathbf{P})^2 + \beta \mathbf{P} \cdot \nabla \phi \right\}. \quad (9)$$

This is a generalization of the free energy functional for active binary mixtures defined in⁴⁸. The first term allows for the segregation of the two phases when the bulk energy density $a > 0$, so that free energy has two minima at $\phi = 0, \phi_0$. The second and third terms determine the interfacial tension. Notice that here a negative value of k_ϕ favours the formation of interfaces while a positive value of c is used to guarantee thermodynamic stability⁵¹. Lowering k_ϕ from positive to negative values leads the system to move from pure ferromagnetic phase to configurations where interfaces between components are favoured^{53–57}. In the Appendix *Adimensional Numbers* we will show that, for a symmetric composition of the mixture, the system sets into a lamellar phase modulated at wavenumber $\kappa = \sqrt{|k_\phi|/2c}$, when $a < k_\phi^2/4c + \beta^2/k_p$ (see

panels (a) and (b) of Fig. 1 for typical lamellar morphology).

The bulk properties of the polar liquid crystal are instead controlled by the $|\mathbf{P}|^2$ and $|\mathbf{P}|^4$ terms, multiplied by the positive constant α . The choice of ϕ_{cr} has been made in order to break the symmetry between the two phases and confine the polarization field in the active phase, $\phi > \phi_{cr}$. The term proportional to $(\nabla \mathbf{P})^2$ describes the energy cost due to elastic deformation in the liquid crystalline phase, gauged to the theory through the elastic constant k_p (a more general treatment can be found in⁵⁸). Finally, the last term takes into account the orientation of the polarization at the interface of the fluid. If $\beta \neq 0$, \mathbf{P} preferentially points perpendicularly to the interface (normal anchoring): towards the passive (active) phase if $\beta > 0$ ($\beta < 0$). A plot of the typical polarization field configuration to interfaces in the lamellar phase is shown with white arrows in panel (e) of Fig. 1. This allows for the confinement of the active behaviour on small scales in a low-Reynolds number environment, offering a way to control the typical length-scales of energy injection – an actual challenge for experiments in the field²¹. The model exhibits a wide phe-

nomenology at varying the activity parameter ζ^{43} , that has been summarized at the beginning of Sect. 3.

2.1 Numerical Method and Parameters

The equations of motion of the polar active emulsion, Eqs. (1)-(3), are solved by means of a hybrid lattice Boltzmann (LB) scheme, which combines a predictor-corrector LB treatment for the Navier-Stokes equation⁵⁹ with a finite-difference predictor-corrector algorithm to solve the order parameters dynamics, implementing a first-order upwind scheme, for the convection term, and fourth-order accurate stencil for the computation of space derivatives.

In this approach the evolution of the fluid is described in terms of a set of distribution functions $f_i(\mathbf{r}_\alpha, t)$ (with index i labelling different lattice directions, thus ranging from 1 to 9) defined on each lattice site \mathbf{r}_α . Their evolution follows a discretized predictor-corrector version of the Boltzmann equation in the BGK approximation:

$$f_i(\mathbf{r}_\alpha + \xi_i \Delta t) - f_i(\mathbf{r}_\alpha, t) = -\frac{\Delta t}{2} [\mathcal{C}(f_i, \mathbf{r}_\alpha, t) + \mathcal{C}(f_i^*, \mathbf{r}_\alpha + \xi_i \Delta t, t)]. \quad (10)$$

Here $\{\xi_i\}$ is the set of discrete velocities, that for the $d2Q9$ model are $\xi_0 = (0, 0)$, $\xi_{1,2} = (\pm u, 0)$, $\xi_{3,4} = (0, \pm u)$, $\xi_{5,6} = (\pm u, \pm u)$, $\xi_{7,8} = (\pm u, \pm u)$, where u is the lattice speed. The distribution functions f_i^* are first-order estimations to $f_i(\mathbf{r}_\alpha + \xi_i \Delta t)$ obtained by setting $f_i^* \equiv f_i$ in Eq. (10), and $\mathcal{C}(f, \mathbf{r}_\alpha, t) = -(f_i - f_i^{eq})/\tau + F_i$ is the collisional operator in the BGK approximation expressed in terms of the equilibrium distribution functions f_i^{eq} and supplemented with an extra forcing term for the treatment of the anti-symmetric part of the stress tensor. The density and momentum of the fluid are defined in terms of the distribution functions as follows:

$$\sum_i f_i = \rho \quad \sum_i f_i \xi_i = \rho \mathbf{v}. \quad (11)$$

The same relations also hold for the equilibrium distribution functions, thus ensuring mass and momentum conservation. In order to correctly reproduce the Navier-Stokes equation we impose the following condition on the second moment of the equilibrium distribution functions:

$$\sum_i f_i \xi_i \otimes \xi_i = \rho \mathbf{v} \otimes \mathbf{v} - \tilde{\sigma}^{bin} - \tilde{\sigma}_s^{pol}, \quad (12)$$

and on the force term:

$$\begin{aligned} \sum_i F_i &= 0, \\ \sum_i F_i \xi_i &= \nabla \cdot (\tilde{\sigma}_a^{pol} + \tilde{\sigma}^{act}), \\ \sum_i F_i \xi_i \otimes \xi_i &= 0, \end{aligned} \quad (13)$$

where we denoted with $\tilde{\sigma}_s^{pol}$ and $\tilde{\sigma}_a^{pol}$ the symmetric and anti-symmetric part of the polar stress tensor, respectively. The equilibrium distribution functions are expanded up to the second or-

der in the velocities:

$$f_i^{eq} = A_i + B_i(\xi \cdot \mathbf{v}) + C_i|\mathbf{v}|^2 + D_i(\xi \cdot \mathbf{v})^2 + \tilde{G}_i : (\xi \otimes \xi). \quad (14)$$

Here coefficients $A_i, B_i, C_i, D_i, \tilde{G}_i$ are to be determined imposing conditions in Eqs. (11) and (12). In the continuum limit the Navier-Stokes equation is restored if $\eta_0 = \tau/3$.

We made use of a parallel approach implementing Message Passage Interface (MPI) to parallelize the code. We divided the computational domains in slices, and assigned each of them to a particular task in the MPI communicator. Non-local operations (such as derivatives), have been treated through the *ghost-cell* approach⁶⁰.

Simulations have been performed on square lattice of size $L = 256$. The concentration ϕ ranges from $\phi \simeq 0$ (passive phase) to $\phi \simeq 2$ (active phase). Unless otherwise stated, parameter values are $a = 4 \times 10^{-3}$, $k_\phi = -6 \times 10^{-3}$, $c = 10^{-2}$, $\alpha = 10^{-3}$, $k_P = 10^{-2}$, $\beta = 0.01$, $\Gamma = 1$, $\xi = 1.1$, $\phi_0 = 2.0$, and $\eta_0 = 1.67$. All quantities in the text are reported in lattice units. We initialized the system starting from a uniform phase, with $\phi(\mathbf{r}) = \langle \phi \rangle + \delta\phi(\mathbf{r})$, where $\langle \phi \rangle = \phi_{cr}$ is the conserved (area) averaged value of the concentration field and $\delta\phi$ is a small perturbation field favouring phase separation and ranging in $[-\frac{\phi_{cr}}{10}, \frac{\phi_{cr}}{10}]$. The initial condition for the polarization field is completely random, being its orientation randomly distributed in the plain, while its intensity is randomly chosen in $[0, 1]$.

Our choice of parameters is such that the Schmidt number ($Sc = \frac{\eta_0}{\rho D}$ where $D = 2Ma/\phi_{cr}^4$ is the diffusion constant) is fixed at values typical for liquids, ~ 2000 where, in absence of activity, lamellae show low resistance to the flow and can easily order. It was shown in⁵⁷ that at smaller Sc lamellar domains hardly align to the flow and may eventually undergo pearling instability, persistent even in the long dynamics.

We considered flow in a channel with no-slip boundary conditions at the top and the bottom walls ($y = 0$ and $y = L$), implemented by bounce-back boundary conditions for the distribution functions⁶¹, and periodic boundary conditions in the y direction. The flow is driven by moving walls, respectively with velocity v_w for the top wall and $-v_w$ for the bottom wall, so that the shear rate is given by $\dot{\gamma} = \frac{2v_w}{L}$.

Moreover neutral wetting boundary conditions were enforced by requiring on the wall sites that the following relations hold:

$$\nabla_\perp \mu = 0, \quad \nabla_\perp (\nabla^2 \phi) = 0, \quad (15)$$

where ∇_\perp denotes the partial derivative computed normally to the walls and directed towards the bulk of the system. Here the first condition ensures density conservation, the second determines the wetting to be neutral. In the case of bacterial swimmers, it is commonly observed that, close to the boundaries, they orient along the wall direction⁶². In actomyosin solutions, the actin filaments can also be assumed to be anchored parallel to the walls due to focal adhesion⁶³. Therefore, suitable boundary conditions for the polarization \mathbf{P} is a strong anchoring condition with \mathbf{P} aligned parallel to the walls

$$P_\perp|_{\text{walls}} = 0, \quad \nabla_\perp P_\parallel|_{\text{walls}} = 0, \quad (16)$$

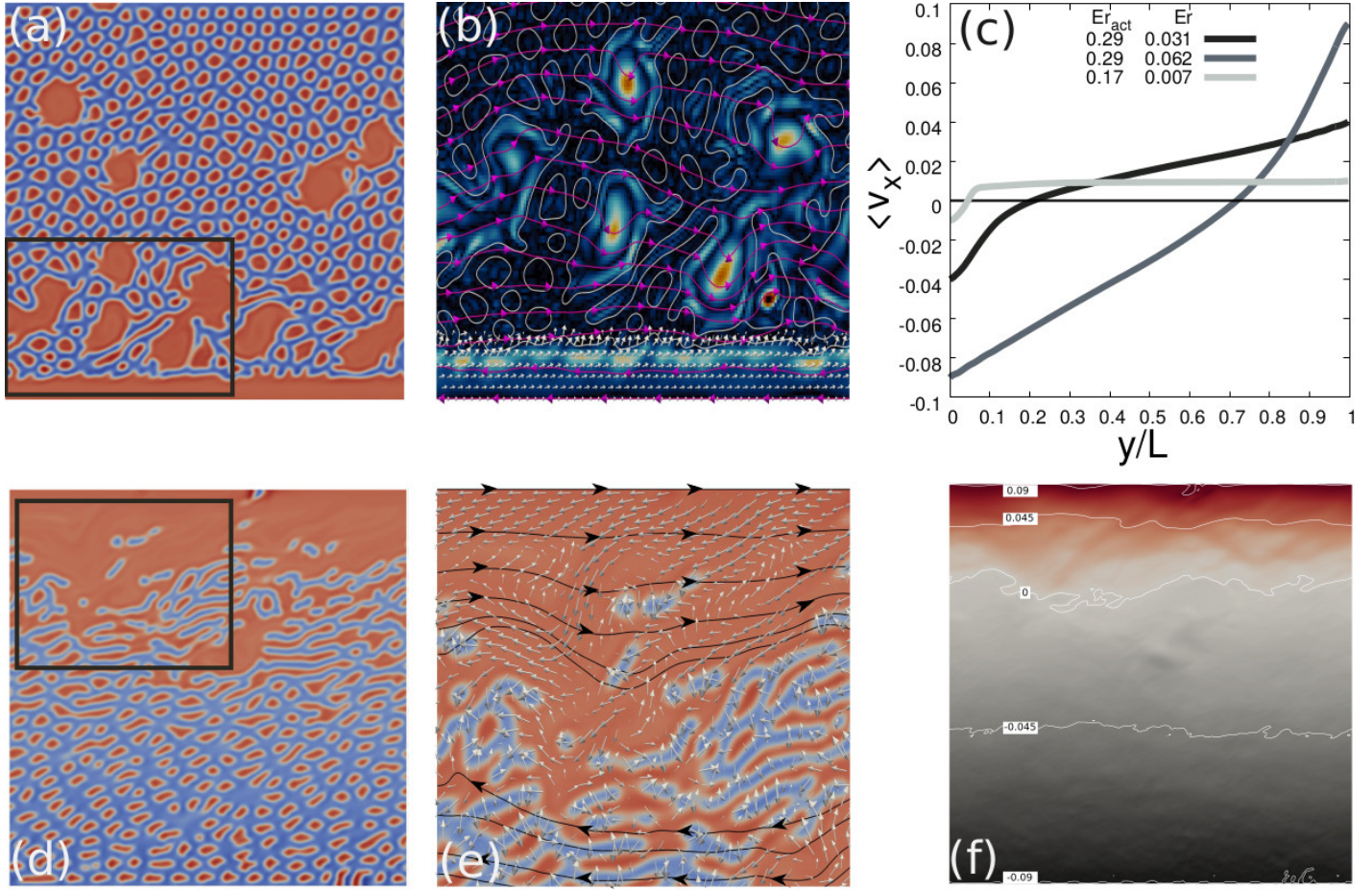


Fig. 2 Unidirectional motion. (a) Concentration contour plot at $Er_{act} = 0.29$, $Er = 0.031$. (b) Contour plot of the vorticity $\omega = (\partial_y v_x - \partial_x v_y)/2$ (black corresponds to $\omega = 0$ and red to $\omega = 10^{-2}$) in the region framed with black box in panel (a); purple lines represent velocity streamlines while the polarization field is plotted in white (for graphical clarity, only in the bottom active layer). (d) Contour plot of the concentration field at $Er_{act} = 0.29$ and $Er = 0.062$ and (e) zoom of the region framed with black box in panel (d), with black lines representing v streamlines and \mathbf{P} plotted in white. (f) Contour plot of the velocity field in the flow direction for the same case shown in panel (d), with few isolines plotted in white. Panel (c) shows $\langle v_x \rangle$ for the two cases considered and also for the case at $Er_{act} = 0.172$, $Er = 0.0075$.

where P_{\perp} and P_{\parallel} denote, respectively, normal and tangential components of the polarization field with respect to the walls. In order to compare external and active forcing in our system, we make use of the Ericksen number, Er , and the active Ericksen number Er_{act} as relevant adimensional quantities. The former is often used in the study of liquid crystals to describe the deformation of the orientational order parameter field under flow and it is defined as the ratio of the viscous stress to the elastic stress. In particular in lamellar systems a suitable choice is given by:

$$Er = \frac{\eta_0 \dot{\gamma}}{B}, \quad (17)$$

where B is the lamellar compression modulus – namely the energy cost for the variation of the lamellar width $\lambda = 2\pi/\kappa$ per unit length, whose expression in terms of the parameter of the model is explicitly derived in the Appendix A. The active Ericksen number, suggested by Giomi for the first time in⁶⁴, is, in turn, defined as the ratio between the module of the activity parameter

ζ and the compression modulus:

$$Er_{act} = \frac{|\zeta|}{B}. \quad (18)$$

3 Linear flow and symmetry breaking transition

Before presenting specific results case we summarize the morphological phenomenology arising in an active extensile polar lamellar system at varying the activity parameter ($\zeta > 0$) in absence of any external forcing. Bonelli *et al.*⁴³ showed that the shear-free system is characterized by a transition at $Er_{act} \approx 0.11$ from the lamellar phase to an emulsion with moving active droplets. The bending instability, typical of extensile gels²⁵, favors this rearrangement. For $Er_{act} \gtrsim 1$ the system enters in a totally mixed phase, characterized by chaotic velocity patterns²⁸. The following Sections will be devoted to present the different behaviours of the sheared system at varying both the intensity of active and external forcing.

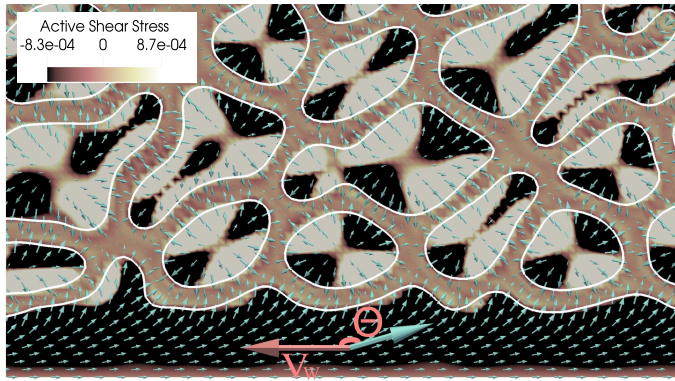


Fig. 3 Active shear stress close to a wall at $Er = 0.0074$, $Er_{act} = 0.172$. The polarization field \mathbf{P} (cyan arrows) exhibits a splayed profile under the mutual effect of strong anchoring to the wall (tangential) and to the interface (homeotropic), while the red arrow shows the direction of the imposed velocity v_w . The angle θ denotes the local orientation of the polarization, sketched by the magnified reference cyan arrow, with respect to the flow. White lines trace the interface ($\phi = \phi_{cr}$) between active and passive phases. Passive (beige) regions are almost stress free, while negative stress in the boundary layer (black) corresponds to a net force opposite to the flow direction. Droplets have quadrupolar structures.

3.1 Linear velocity profiles and lamellar phase.

The scenario just described is strongly influenced by an external shear flow. Due to the tendency of lamellae to align with the flow, an applied shear, even small, is found to counter activity-induced bending, thus extending the range of stability of lamellar order towards larger Er_{act} ($Er_{act} \lesssim 0.18$) with respect to its unsheared counterpart. Under this threshold and for a vast range of shear rates, the system sets into a lamellar phase, as shown in panels (a) and (d) of Fig. 1. The region with these properties is red in Fig. 8, where flow regimes found by scanning the $Er - Er_{act}$ plane are summarized. At small shear, relaxation dynamics leads to the formation of long-lived dislocations in the lamellar pattern, as the one highlighted by the black box in panel (a) of Fig. 1. Panel (b) of the same Figure shows the detail of the velocity field in the neighborhood of the dislocation. If $\dot{\gamma}$ is weak enough, defects are capable to consistently alterate the velocity pattern, since dislocations develop flows trasversal to the direction of lamellar-alignment, thus leading to permanent shear bandings in the velocity profile (as shown by the red line in the inset of Fig. 1c). At greater values of shear rate, the superimposed flow is strong enough to eliminate dislocations (see for example panel (d) in Fig. 1 and Movie 1), eventually leading to the formation of disruptions that are much less effective on the flow than dislocations, as confirmed by the linear behaviour of the corresponding velocity profile. In this regime lamellae are globally aligned to the flow, while the polarization field, homeotropically anchored to the interfaces (panel (e) of Fig. 1), is pointing towards the passive phase (blue regions in zoom of panel (e)). Panel (f) compares the time evolution of shear stress for the two cases considered. Dynamics at high shear leads to a smoother and faster relaxation towards lower values of σ_{xy} . When the imposed shear is weaker, oscillations or jumps, as the one marked by an arrow at $t = 6 \times 10^6$ in panel (f) of Fig. 1, are due to the annihilation of two dislocations.

3.2 Unidirectional motion.

The behaviour becomes more complex when activity is increased. The combination of activity and shear has dramatic consequences. The system undergoes a morphological transition from the lamellar phase towards an emulsion of active material in a passive background, a behaviour also found by Bonelli *et al.*⁴³ at lower active dopings. Fig. 2 shows two cases at $Er = 0.031$, $Er_{act} = 0.29$ (top row) and $Er = 0.062$, $Er_{act} = 0.29$ (bottom row) characterized by the formation of a thick layer of material close to one boundary (see dynamics in Movie 2), and small features on Brazovskii lengthscale $\lambda = 2\pi/\kappa$ coexisting with larger aggregates of active material elsewhere. Such symmetry breaking is mediated and sustained by the formation of these large active domains where bending polarization instabilities, typical of extensile systems, act as a source of vorticity (see panel (b)). Big active domains are mostly advected by the intense flow close to the walls, as shown by purple velocity streamlines, differently from what happens in shear-free systems where polarization bending results into the rotational motion of the bigger active droplets. Fig. 2c shows the related x -averaged velocity profile $\langle v_x \rangle$ (grey curve): Instead of the linear behaviour of Fig. 1c, one observes banded flows with the higher gradient in correspondence of the wall with the active layer. Similar cases occur at different Er, Er_{act} with deposition of active material randomly on the top or bottom wall. Streamlines of \mathbf{v} (in panels (b) and (e) of Fig. 2) show that the inversion of the fluid velocity takes place in correspondance of the interface of the active layer. The top-bottom symmetry breaking leads to a net flux of matter in the flow direction and has been named *unidirectional motion*. Cases exhibiting such property have been plotted in grey in Fig. 8. Moreover, as shear is increased, the position of flow inversion migrate towards the bulk of the system (see the dark grey profile at the larger Er in panel (c) and the corresponding v_x contour plot in panel (f)). Unidirectional flow (grey region in Fig. 8) may occur with almost everywhere vanishing gradient of $\langle v_x \rangle$, and in this case it will be called *superfluidic*^{32,65} (see light grey profile in Fig. 2c).

Which are the mechanisms for the observed velocity profiles? And how to explain the flow symmetry breaking transition? Due to complexity of the system we can only partially answer to these questions. The velocity behaviour is strictly related to that of polarization close to the walls. Thick layers as the one in Fig. 2a,d and in Fig. 3 are characterized by the bending of polarization due to competition between strong parallel anchoring to the walls and perpendicular orientation to domain interfaces, leading to a negative active shear stress contribution. This is clearly shown in Fig. 3, where white/black regions correspond to positive/negative values and correspond to active domains, while beige ones are associated to the isotropic background and correspond to almost null values. Moreover, topological defects in the active layer are strongly inhibited by elastic energy, as suggested by the uniform polarization pattern in the black bottom layer.

Within the active layer $\sigma_{xy}^{act} \sim \frac{\zeta}{2} \phi_0 (P_{eq})^2 \sin 2\theta$, where θ denotes the local orientation of polarization with respect to the imposed velocity ($0 \leq \theta \leq \pi$), thus generating an active force density in

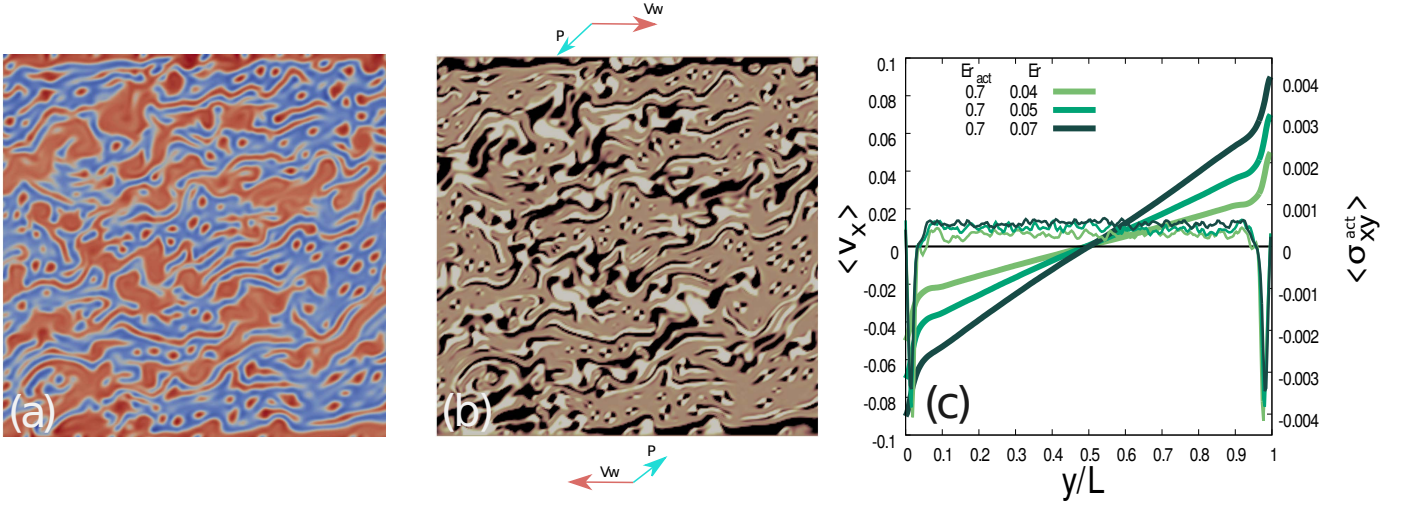


Fig. 4 Symmetric shear thinning profiles. Concentration (a) and active shear stress (b) contour plot for the case at $Er_{act} = 0.70, Er = 0.04$. The colour code is the same of Fig.3. Red arrows denote the direction of the moving walls, and cyan ones the direction of the polarization, averaged within the active layers close to the walls. (c) Velocity $\langle v_x \rangle$ (thick lines) and active shear stress profiles $\langle \sigma_{xy}^{act} \rangle$ (thin) averaged along the flow direction, for the case corresponding to panels (a) and (b) and analogous ones.

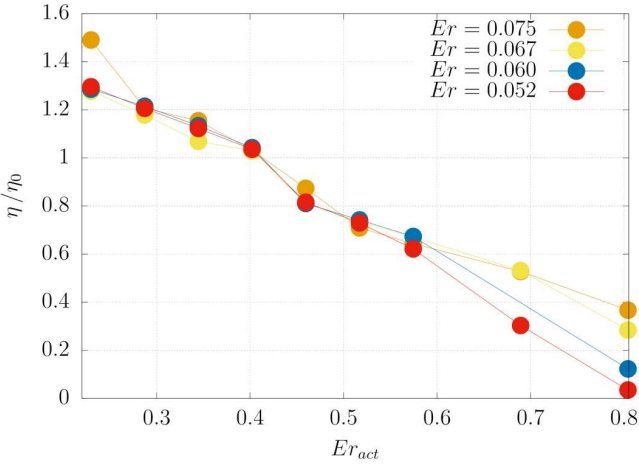


Fig. 5 Shear thinning in extensile mixtures. Ratio between apparent viscosity η (measured as $\langle \sigma_{xy}^{tot} \rangle / \dot{\gamma}$) and shear viscosity η_0 , while varying activity for some values of the Ericksen number.

the flow direction ($f_{\parallel}^{act} = \partial_{\perp} \sigma_{xy}^{act}$, where ∂_{\perp} denotes derivative in the direction normal to the walls). This can either reinforce the imposed flow if the polarization field is oriented as v_w (since $\partial_{\perp} \sin 2\theta > 0$), or lead to a reduction of the fluid velocity if opposite (since $\partial_{\perp} \sin 2\theta < 0$). However, between the two possible orientations, the one reinforcing the flow does not appear in the cases discussed so far. In order to clarify this point we define the average polarization P_w on each wall – it can be calculated as $P_w \sim \langle P_{\parallel} |_{walls} \rangle$, where here $\langle \cdot \rangle$ stands for the average over few layers close to the wall sites. For the unidirectional motion case, P_w is null at the wall where the thick active layer is absent, so that we denote such polarization state as $\mathbf{0}$. If the polarization is opposite to v_w , as in the bottom/top of panel (b)/(e) of Fig. 2, we will indicate it with $-$. Following the notation just introduced, we will refer to the global states shown in Fig. 2 with $\mathbf{0-}$, independently of the top-bottom asymmetry.

3.3 Symmetric shear thinning profiles.

By further increasing both activity and shear rate, phase demixing is more pronounced (Fig. 4a) with the formation of an emulsions of amorphous active domains in a passive matrix. Active layers form on *both* walls so that symmetry is restored also at level of the velocity profiles $\langle v_x \rangle$, with gradients in the bulk of the system lower than the imposed one, as shown in panel c of Fig. 4 (thick lines). Symmetric cases exhibiting such phenomenology have been plotted in green in Fig. 8. Under these conditions, it may happen that the velocity gradient in the bulk of the system is either everywhere vanishing or, eventually, opposite to the one externally imposed (*negative viscosity*), despite such states are found to be unstable in the long term (see Sec. 4). To explain the flow properties presented, we analyse the active shear stress profiles $\langle \sigma_{xy}^{act} \rangle$ averaged in the flow direction (see thin lines in panel (c)). This confirms that the active stress is considerably different from zero only in the layer close to both walls, where it assumes negative values – thus leading to the sharp decrease of the intensity of the flow in the same region – while it is approximately null in the bulk. A contour plot of the active stress is also shown in panel b of Fig. 4, clearly showing that the P_w polarization state at boundaries is in a $-$ configuration.

Such behaviour is also accompanied by shear thinning, typical of extensile fluids as Er_{act} is increased. This is analyzed in Fig. 5 where the ratio between the apparent viscosity $\eta = \langle \sigma_{xy}^{tot} \rangle / \dot{\gamma}$ (where $\langle \sigma_{xy}^{tot} \rangle$ denotes the time average of the total stress tensor), and the shear viscosity η_0 has been plotted versus Er_{act} . We varied Er in the range $Er \gtrsim 0.05$, where viscosity states are found to be stable for any value of Er_{act} . Viscosity mainly depends on the intensity of the active doping, while no substantial dependence is found on the shear rate if $Er_{act} \lesssim 0.6$. This suggests that activity, inducing shear thinning, is a parameter capable of controlling the rheological property of extensile suspensions.

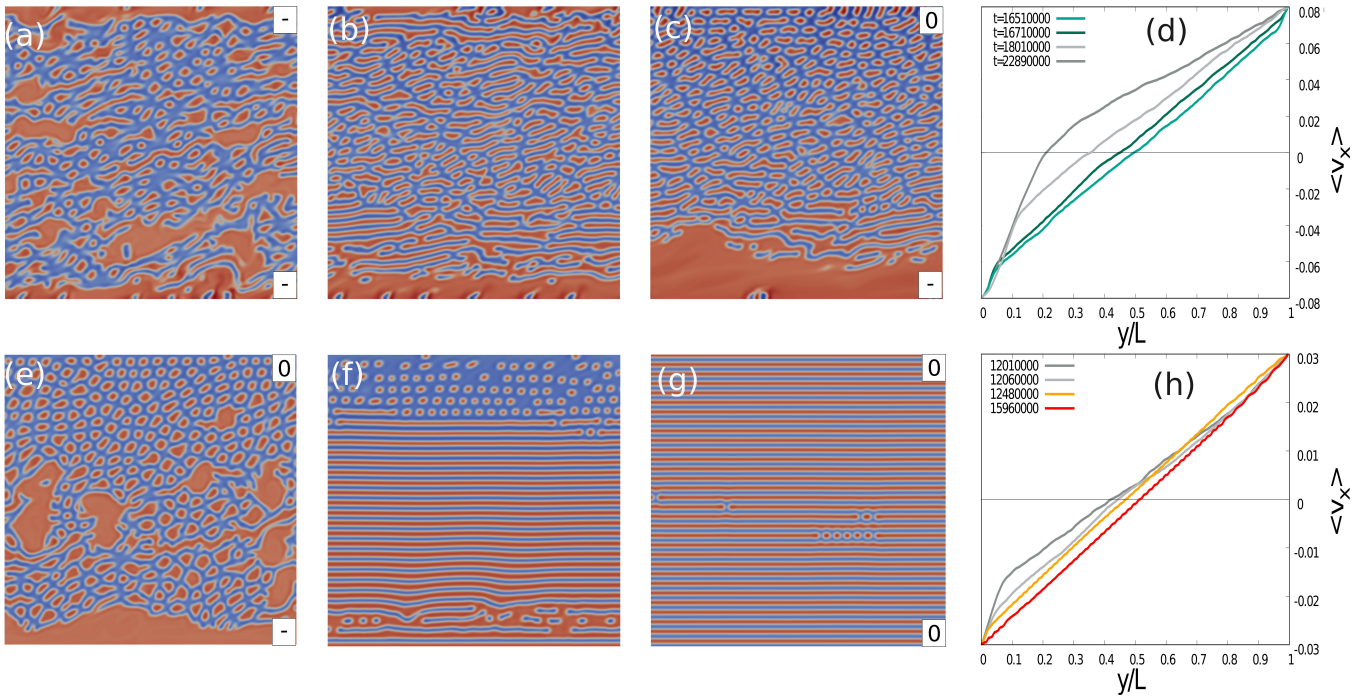


Fig. 6 Activity quench. Panels (a)-(c) show the evolution of the system after that Er_{act} has been quenched from 0.57 to 0.28, thus moving from the green region of Fig. 8 to the grey one, at $Er = 0.06$. The colors of the profiles have been chosen in accordance to the color of the corresponding region in the phase diagram of Fig. 8. Labels (0 or -) at the top and at the bottom of initial and final panel denote the state of the polarization at the boundary. The evolution of velocity profiles is also shown in panel (d). Panels (e)-(g) show the same for the quench from the grey region ($Er_{act} = 0.22$) towards the red region ($Er_{act} = 0.057$) of Fig. 8 at $Er = 0.01$, with the evolution of velocity profiles in panel (h). Contour plots correspond to the first, third and last velocity profiles in panels (d) and (h)

3.4 Activity quench.

We further analyzed the nature of the transition between the symmetric configurations at higher activity (green region in Fig. 8) and states with unidirectional flow at weaker activity, starting from a stationary states at $Er_{act} = 0.57$ and quenching the activity to $Er_{act} = 0.28$ at fixed $Er = 0.06$. Panels (a)-(c) in Fig. 6 show the quenching dynamics: starting from the symmetric configuration of panel (a) at $Er_{act} = 0.57$, amorphous active domains progressively stretch in the flow direction and cluster on the bottom boundary (see panel (b)). This accompanies the *melting* of the active layer close to the upper wall, finally generating the asymmetric configuration of panel (c) characterized by unidirectional flow. The evolution of velocity profiles is shown in panel (d). Panels (e)-(g) show the results of a similar experiment: this time we quenched the active parameter so to move from the grey region ($Er_{act} = 0.22$) with unidirectional motion, to the red one ($Er_{act} = 0.057$) with linear profiles, in Fig. 8, while keeping shear rate fixed at $Er = 0.01$. After the quench droplets are no more stable, since the active doping is not strong enough to maintain the bending instability. A lamellar phase progressively grows from the bottom of the system, where most of the active material was initially found, towards the upper wall. The final configuration is characterized by a symmetric, defect-free lamellar configuration, with linear velocity profile, whose evolution can be appreciated by looking at panel (h).

4 Intermittent flow

Surprisingly, yet another behaviour appear in a vast region of the parameter plane at small shear, $Er \lesssim 0.04$, and sufficiently large activity, $Er_{act} \gtrsim 0.4$, (blue in Fig. 8). Under this condition, the system is symmetric and exhibits an intermittent flow regime. This is to be related, once again, to the polarization state at the boundaries. Indeed, this time we find (unstable) configurations where P_w is oriented in the same direction of the imposed velocity, so that we will denote such state as $+$. The dynamics of the system is characterized by jumps between $++$, $-+$ and $--$ states.

Such intermittent behaviour is reflected in the evolution of the area averaged stress, as shown in Fig. 7a. Elastic contributions are on average constant, while active stress fluctuates around positive, negative or vanishing values. These are found to be largely determined by the portion of the system closer to boundaries (see Fig. 7c). For each wall the sign of active stress coincides with the one of P_w , so that positive and negative total stress correspond respectively to $++$ and $--$ P_w states, while total zero active stress comes from opposite P_w contributions ($-+$ states). Viscosity jumps (Fig. 7 a) correspond to the inversion of the polarization on one of the two walls during evolution. The inversion of polarization on the boundaries, generally prevented by elastic effects and strong anchoring, can occur as a result of *catastrophic* events, such as collision of big domains with the active layer (see Appendix B, and Movie 3,4). $--$ states typically live longer than others, as can be appreciated looking at the pdf of the total shear stress reported in Fig. 7b. The statistics of viscosity states has been

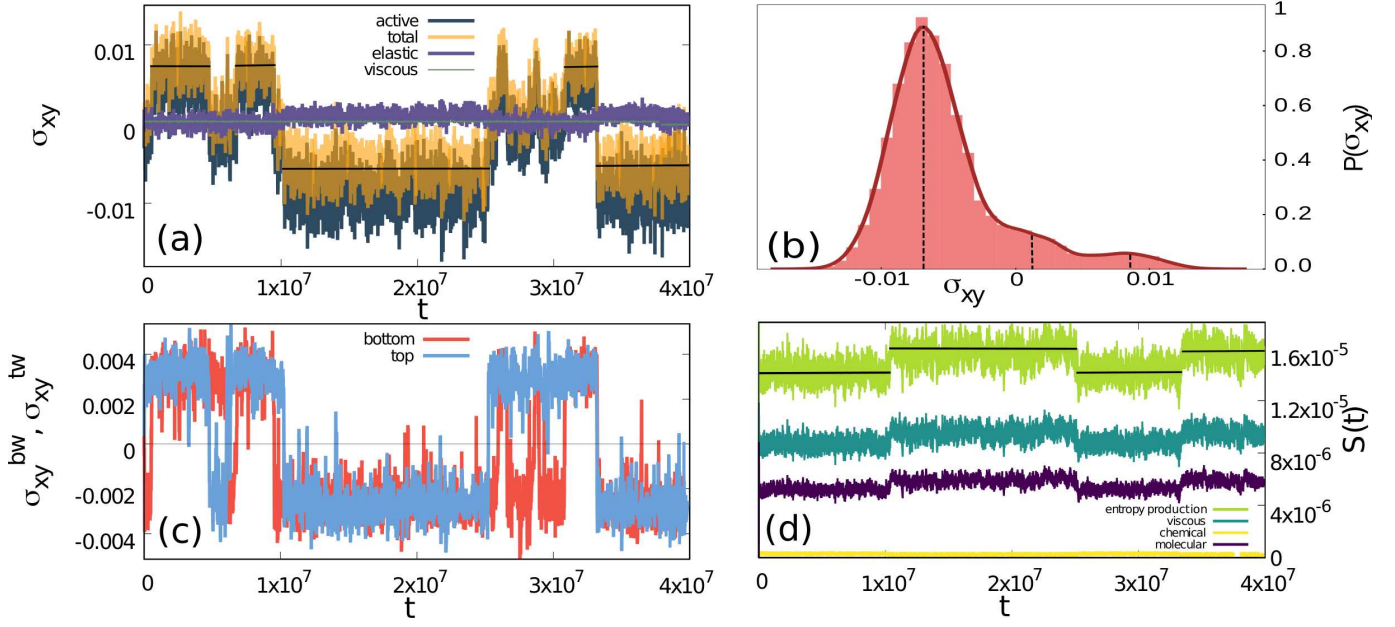


Fig. 7 Entropy production in multistable states. (a) Time evolution of stress contributions at $Er_{act} = 1.14, Er = 0.00075$. The total stress is plotted in transparent yellow, while the active one is the dark blue curve underneath. Panel (b) shows the *pdf* of the total stress (data from 40 independent runs, fitted by 3 normal distributions peaked at $\sigma_{xy} = -0.0068, 0.0009, 0.0086$). (c) Total stress close to bottom and top walls, respectively computed as $\sigma_{xy}^{tw} = \int dx \int_{Ly-l}^{Ly} dy \sigma_{xy}$ and $\sigma_{xy}^{bw} = \int dx \int_0^l dy \sigma_{xy}$, where l is the width of the layer. Here $l = 15$. Nevertheless, as long as $l < Ly/2$, results remain unaltered. (d) Entropy production. Negative viscosity states, corresponding to -- configurations of polarization at the boundaries, live longer than others. Entropy production $s(t)$ assumes greater values in correspondence of these regions. Each contribution to $s(t)$ has been measured by integrating on the computational domain the terms on the right-hand side of Eq. (27).

constructed considering 40 different runs for the same couple of parameters $Er_{act} = 1.14, Er = 0.0075$. The typical length of each run is of about 10^7 lattice Boltzmann iterations. The data for the shear stress have been sampled under stationary conditions and then fitted with the sum of three normal distributions, centred at values marked with dotted lines in panel (b). These mean values are consistent with the average of the stress in the different states of Fig. 7a, and their probability of occurrence will correspond to the amount of time that the system spends in each of them.

To go deeper in the characterization of this behaviour we measured entropy production during the system time evolution. Generally, in non-equilibrium systems, the entropy density $\Sigma(r, t)$ obeys the continuity equation

$$\partial_t \Sigma + \nabla \cdot (\Sigma \mathbf{v}) = s, \quad (19)$$

where s is the rate of entropy production per unit volume, subject to the condition $s \geq 0$. This can be written in terms of generalized fluxes J_i and forces X_i , as⁶⁶

$$Ts = J_i X_i, \quad (20)$$

with T the temperature – fixed at in our simulations ($T = 0.5$) since we are neglecting heat transfer. Thermodynamic forces are chosen as follows:

$$\tilde{X}_v = (\nabla \mathbf{v})^S \equiv \tilde{D}, \quad (21)$$

$$X_P = -\frac{\delta F}{\delta P} \equiv \mathbf{h}, \quad (22)$$

$$X_\phi = \nabla \frac{\delta F}{\delta \phi} \equiv \nabla \mu, \quad (23)$$

where F is given by Eq. (9), \tilde{D} is the strain rate tensor. Moreover, in our model the following linear phenomenological relations between forces and fluxes hold¹:

$$\tilde{J}_v = \tilde{\sigma}^{tot}, \quad (24)$$

$$J_P = \partial_t P + (\mathbf{v} \cdot \nabla) P + \tilde{\Omega} \cdot P = \frac{1}{\Gamma} \mathbf{h} + \xi \tilde{D} \cdot P, \quad (25)$$

$$J_\phi = -M \nabla \mu, \quad (26)$$

where we denoted with $\tilde{\Omega}$ the vorticity tensor, that is the antisymmetric part of the gradient velocity tensor. By substituting these relations into Eq. (20) we find that

$$Ts = 2\eta \tilde{D} : \tilde{D} + \frac{1}{\Gamma} \mathbf{h} \cdot \mathbf{h} + M(\nabla \phi)^2, \quad (27)$$

where we retained only those terms even under time reversal symmetry. We here identify three contributions: the first one is the entropy production due to viscous effects, $2\eta \tilde{D} : \tilde{D}$, while the second ($\frac{1}{\Gamma} \mathbf{h} \cdot \mathbf{h}$) and the third ($M(\nabla \phi)^2$) ones are respectively the molecular and the chemical terms, accounting for the entropy produced during the relaxation dynamics of P and ϕ . This expression is quadratic in the thermodynamic forces and satisfies all required conditions, among which invariance under Galilean transformations as well as the second principle of thermodynamics. In the stationary regime, entropy production must be equal to the energy injected into the system, due to the work of the walls

and active pumping. We emphasize that activity ζ is a reactive parameter and therefore does not appear in the entropy production formula⁶⁷. However activity influences the dynamics, acting as a velocity source through the active stress, thus contributing indirectly to dissipation.

Panels (a) and (d) compare the behaviour of the stress and entropy production. The evolution of the stress is characterized by two regions of stability of negative viscosity – whose lifetime is $\mathcal{O}(10^7)$ LB iterations – that respectively occur from $t \approx 10^7$ to 2.5×10^7 , and from $t \approx 3.2 \times 10^7$ to 4×10^7 . These states have also the highest probability, as can be appreciated looking at the pdf of the total stress in panel (b) of Fig. 7.

In Panel (d) the different entropy production contributions are shown. We first notice that the contribution due to diffusion/chemical (yellow line) is almost null. In addition, the viscous dissipation (blue line) is always greater than the contribution due to the molecular field (violet line). This suggests that the hydrodynamics of the system – driven by active injection and external forcing – is mainly countered by viscous dissipation phenomena. Moreover, the total entropy production oscillates around two different values and jumps during time evolution, with the highest value corresponding to the negative viscosity states. This behaviour, with prevalence of -- polarization states is typical of all the intermittent cases (blue region in Fig. 8), and is compatible with a maximum entropy production principle (*MaxEPP*). Various variational principles, related to entropy production rates, have been put forward to quantitatively select the most probable state in multi-stable systems. While much efforts have been spent in the search of a general principle and recent progress has been made⁶⁸ on a theoretical derivation of such a principle, questions about how this should be interpreted and applied have not been answered, especially for systems evolving far from thermodynamic equilibrium. In particular, a *MaxEPP* has been implemented as a selection criteria to study systems characterized by multiple non-equilibrium stationary states⁶⁸ and very recently the Schlögl model⁶⁹ – that is a simple, analytically solvable, one-dimensional bistable chemical model – has been used to demonstrate that the steady state with the highest entropy production is favoured⁷⁰. In the system here considered, we found that entropy production $s(t)$ is higher for the most likely -- states, suggesting that *MaxEPP* may act as a thermodynamic principle in selecting non-equilibrium states.

5 Overview, phase diagram and conclusions

The various behaviours found in the active polar emulsion under shear have been summarized in Fig. 8, at varying Er and Er_{act} . At small Er_{act} , the system arranges in a lamellar configuration. In this range, at small shear rates, few persistent defects (dislocations) give rise to slight deformations in velocity profiles (dashed-red region in Fig. 8). Increasing Er , dislocations are washed out by the flow and the system enters the region of linear velocity profiles (red region in Fig. 8). As activity is increased, morphology is characterized by a transition towards asymmetric configurations, with the formation of a thick layer of material close to *one* boundary, thus generating a non-vanishing flux of matter – a behaviour addressed as *unidirectional flow*. Such regime is stable for a broad

range of Er at intermediate active dopings (grey region in Fig. 8). By further increasing activity, at high shear rate, phase demixing is more pronounced and this has important consequences on the flow. Active layers form on *both* walls and symmetry is restored. Under these conditions, it may happen that the velocity gradient in the bulk of the system is either everywhere vanishing or, eventually, opposite to the one externally imposed (*negative viscosity*), despite such states are found to be unstable in the long term. The region with stable symmetric profiles is green in Fig. 8. Cases in the blue region are instead characterized by the jumping dynamics described in the previous section.

We also remark that the results presented in this paper strictly hold for bidimensional geometries – as often happens in experimental realizations of active systems, where bacteria and cytoskeletal suspensions are usually confined at a water-oil interface^{7,27}. In full *3d* environments – where both vortex stretching of the flow field and twisting of the polarization field are allowed – the proliferation of degrees of freedom may strongly affect the behaviour of the system that is indeed different even in absence of any internal and/or external forcing^{71,72}.

In conclusions, we showed how the competition between externally imposed shear and local energy injection results in a wealth of different rheological behaviours, that can be explained in terms of specific dynamical mechanisms. As an example, jumps between velocity profiles with positive and negative gradients are due to collisions between large active droplets or domains and active layers coagulated on the moving walls. The generalized active gel model proposed in this work has allowed us to perform a fully *2d* analysis, by keeping under control the time evolution of the important variables, such as the local concentration and the orientation of the active constituents. Thus we confirmed, by varying both external and internal forcing, the existence of superfluidic and negative viscosity states found experimentally in bacterial suspensions^{36,37} whose first numerical confirmation by means of quasi-*1d* simulations was furnished in⁴⁰. Moreover, we also found that a maximum entropy production principle holds in selecting the most probable state in the intermittent viscosity regime. Since most of the observed behaviours mainly arise due to the elastic properties of the order parameter, they are expected to stay valid also in nematic systems. This because the dynamics of polar systems differs from their nematic counterpart mainly for the allowed topological defects. We hope that this study can stimulate the design of new active materials and devices with pioneering applications.

Conflict of Interest

There are no conflicts of interest to declare

Acknowledgments

Simulations were performed at Bari ReCaS e-Infrastructure funded by MIUR through the program PON Research and Competitiveness 2007-2013 Call 254 Action I. A.T. acknowledges funding from the European Research Council under the European Union's Horizon 2020 Framework Programme (No. FP/2014-2020) ERC Grant Agreement No.739964 (COPMAT). We thank Davide Marenduzzo and Ilario Favuzzi for the useful discussions.

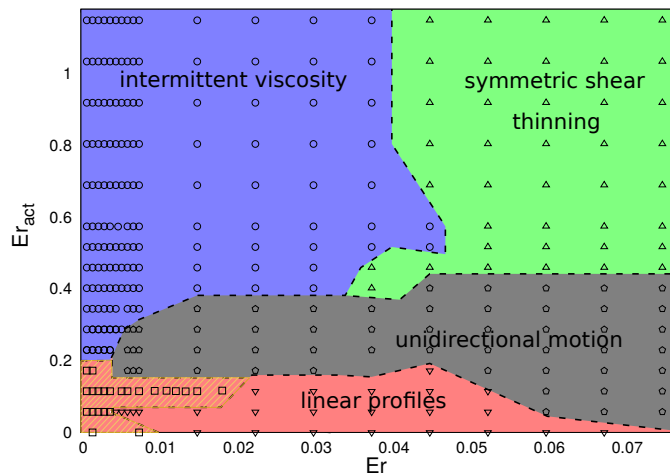


Fig. 8 Flow regimes in the E_r - $E_{r_{act}}$ plane, as described in the text. Hollow marks denote simulation points.

Notes and references

- 1 K. Kruse, J.-F. Joanny, F. Jülicher, J. Prost, and K. Sekimoto. Asters, Vortices, and Rotating Spirals in Active Gels of Polar Filaments. *Phys. Rev. Lett.*, 92:078101, 2004.
- 2 J.-F. Joanny and J. Prost. Active gels as a description of the actin-myosin cytoskeleton. *HFSP j.*, 3(2):94–104, 2009.
- 3 M.C. Marchetti, J.-F. Joanny, S. Ramaswamy, T.B. Liverpool, J. Prost, M. Rao, and R.A. Simha. Hydrodynamics of soft active matter. *Rev. Mod. Phys.*, 85:1143, 2013.
- 4 A. Sokolov, M. Apodaca, B.A. Grzybowski, and S. Aranson. Swimming bacteria power microscopic gears. *Proc. Natl. Acad. Sci. USA*, 107(3):969–974, 2010.
- 5 R. Di Leonardo, L. Angelani, D. Dell’Arciprete, G. Ruocco, V. Iebba, S. Schippa, M.P. Conte, F. Mecarini, F. De Angelis, and E. Di Fabrizio. Bacterial ratchet motors. *Proc. Natl. Acad. Sci. USA*, 107(21):9541–9545, 2010.
- 6 J.M. Yeomans. Playful topology. *Nat. Mater.*, 13, 2014.
- 7 A. Doostmohammadi, J. Ignés-Mullol, J.M. Yeomans, and F. Sagués. Active nematics. *Nat. Commun.*, 9, 2018.
- 8 D. Needleman and Z. Dogic. Active matter at the interface between materials science and cell biology. *Nat. Rev. Mater.*, 2, 2017.
- 9 T. Vicsek and A. Zafeiris. Collective motion. *Phys. Rep.*, 517(3):71 – 140, 2012.
- 10 W.C.K. Poon. *From Clarkia to Escherichia and Janus: The physics of natural and synthetic active colloids*, volume 184 of *Proceedings of the International School of Physics "Enrico Fermi"*. C. Bechinger and F. Sciortino and P. Ziherl, 2013.
- 11 J. Elgeti, R.G. Winkler, and G. Gompper. Physics of microswimmers-single particle motion and collective behavior: a review. *Rep. Prog. Phys.*, 78:056601, 2015.
- 12 M.E. Cates and J. Tailleur. Motility-Induced Phase Separation. *Annu. Rev. Condens. Matter Phys.*, 6:219–244, 2015.
- 13 E. Kanso and D. Saintillan. Special Issue Editorial: Emergent Collective Behavior: From Fish Schools to Bacterial Colonies. *J. Nonlinear Sci.*, 25(5):1051–1052, 2015.
- 14 C. Bechinger, R. Di Leonardo, H. Löwen, C. Reichhardt, G. Volpe, and G. Volpe. Active particles in complex and crowded environments. *Rev. Mod. Phys.*, 88:045006, 2016.
- 15 J.M. Yeomans. The hydrodynamics of active systems. *Nuovo Cimento D*, 40(01):1 – 31, 2017.
- 16 G. Gonnella, D. Marenduzzo, A. Suma, and A. Tiribocchi. Motility-induced phase separation and coarsening in active matter. *C. R. Phys.*, 16:316, 2015.
- 17 P. Digregorio, D. Levis, A. Suma, L.F. Cugliandolo, G. Gonnella, and I. Pagonabarraga. Full Phase Diagram of Active Brownian Disks: From Melting to Motility-Induced Phase Separation. *Phys. Rev. Lett.*, 121:098003, 2018.
- 18 T. Surrey, F. Nédélec, S. Leibler, and E. Karsenti. Physical Properties Determining Self-Organization of Motors and Microtubules. *Science*, 292:1167, 2001.
- 19 J. Prost, F. Jülicher, and J.-F. Joanny. Active gel physics. *Nat. Phys.*, 11(2):111, 2015.
- 20 P. Guillamat, J. Ignés-Mullol, and F. Sagués. Control of active liquid crystals with a magnetic field. *Proc. Natl. Acad. Sci. USA*, 113(20):5498, 2016.
- 21 T. Sanchez, D.T.N. Chen, S.J. Decamp, M. Heymann, and Z. Dogic. Spontaneous motion in hierarchically assembled active matter. *Nature*, 491:431–434, 2012.
- 22 C. Dombrowski, L. Cisneros, S. Chatkaew, R.E. Goldstein, and J.O. Kessler. Self-Concentration and Large-Scale Coherence in Bacterial Dynamics. *Phys. Rev. Lett.*, 93:098103, 2004.
- 23 H.P. Zhang, A. Be’er, E.L. Florin, and H.L. Swinney. Collective motion and density fluctuations in bacterial colonies. *Proc. Natl. Acad. Sci. USA*, 107(31):13626–13630, 2010.
- 24 S. Ramaswamy. The Mechanics and Statistics of Active Matter. *Annu. Rev. Condens. Matter Phys.*, 1:323, 2010.
- 25 R.A. Simha and S. Ramaswamy. Hydrodynamic Fluctuations and Instabilities in Ordered Suspensions of Self-Propelled Particles. *Phys. Rev. Lett.*, 89:058101, 2002.
- 26 D. Marenduzzo, E. Orlandini, and J.M. Yeomans. Hydrodynamics and Rheology of Active Liquid Crystals: A Numerical Investigation. *Phys. Rev. Lett.*, 98:118102, 2007.
- 27 H.H. Wensink, J. Dunkel, S. Heidenreich, K. Drescher, R.E. Goldstein, H. Lowen, and J.M. Yeomans. Meso-scale turbulence in living fluids. *Proc. Natl. Acad. Sci. USA*, 109, 2012.
- 28 G. Gonnella L. Carenza, L. Biferale. Multi-scale control of active emulsion dynamics. *arXiv:1906.05968*, 2019.
- 29 D. Saintillan. Rheology of Active Fluids. *Annu. Rev. Fluid Mech.*, 50(1):563–592, 2018.
- 30 M.E. Cates and E. Tjhung. Theories of binary fluid mixtures: from phase-separation kinetics to active emulsions. *J. Fluid Mech.*, 836:P1, 2018.
- 31 Y. Hatwalne, S. Ramaswamy, M. Rao, and R.A. Simha. Rheology of Active-Particle Suspensions. *Phys. Rev. Lett.*, 92:118101, 2004.
- 32 M.E. Cates, S.M. Fielding, D. Marenduzzo, E. Orlandini, and J.M. Yeomans. Shearing Active Gels Close to the Isotropic-Nematic Transition. *Phys. Rev. Lett.*, 101:068102, 2008.
- 33 A. Sokolov and I.S. Aranson. Reduction of Viscosity in Sus-

- pension of Swimming Bacteria. *Phys. Rev. Lett.*, 103:148101, 2009.
- 34 J. Gachelin, G. Mino, H. Berthet, A. Lindner, A. Rousselet, and E. Clément. Non-Newtonian Viscosity of Escherichia coli Suspensions. *Phys. Rev. Lett.*, 110:268103, 2013.
 - 35 L. Giomi, T.B. Liverpool, and M.C. Marchetti. Sheared active fluids: Thickening, thinning, and vanishing viscosity. *Phys. Rev. E*, 81:051908, 2010.
 - 36 H.M. López, J. Gachelin, C. Douarche, H. Auradou, and E. Clément. Turning Bacteria Suspensions into Superfluids. *Phys. Rev. Lett.*, 115:028301, 2015.
 - 37 S. Guo, D. Samanta, Y. Peng, X. Xu, and X. Cheng. Symmetric shear banding and swarming vortices in bacterial superfluids. *Proc. Natl. Acad. Sci. USA*, 2018.
 - 38 H. Wioland, E. Lushi, and R.E. Goldstein. Directed collective motion of bacteria under channel confinement. *New J. Phys.*, 18(7):075002, 2016.
 - 39 K.-T. Wu, J.B. Hishamunda, D.T.N. Chen, S.J. DeCamp, Y.-W. Chang, A. Fernández-Nieves, S. Fraden, and Z. Dogic. Transition from turbulent to coherent flows in confined three-dimensional active fluids. *Science*, 355(6331), 2017.
 - 40 A. Loisy, J. Eggers, and T.B. Liverpool. Active Suspensions have Nonmonotonic Flow Curves and Multiple Mechanical Equilibria. *Phys. Rev. Lett.*, 121:018001, 2018.
 - 41 S. Rafaï, L. Jibuti, and P. Peyla. Effective Viscosity of Microswimmer Suspensions. *Phys. Rev. Lett.*, 104:098102, 2010.
 - 42 G. Foffano, J.S. Lintuvuori, A.N. Morozov, K. Stratford, M.E. Cates, and D. Marenduzzo. Bulk rheology and microrheology of active fluids. *Eur. Phys. J. E*, 35:98, 2012.
 - 43 F. Bonelli, L.N. Carenza, G. Gonnella, D. Marenduzzo, E. Orlandini, and A. Tiribocchi. Lamellar ordering, droplet formation and phase inversion in exotic active emulsions. *Sci. Rep.*, 9:2801, 2019.
 - 44 G. Negro, L.N. Carenza, P. Digregorio, G. Gonnella, and A. Lamura. Morphology and flow patterns in highly asymmetric active emulsions. *Physica A*, 503:464 – 475, 2018.
 - 45 J. Schwarz-Linek, C. Valeriani, A. Cacciuto, M.E. Cates, D. Marenduzzo, A.N. Morozov, and W.C.K. Poon. Phase separation and rotor self-assembly in active particle suspensions. *Proc. Natl. Acad. Sci. USA*, 109(11):4052–4057, 2012.
 - 46 E. Tjhung, D. Marenduzzo, and M.E. Cates. Spontaneous symmetry breaking in active droplets provides a generic route to motility. *Proc. Natl. Acad. Sci. U.S.A.*, 109(31):12381–12386, 2012.
 - 47 E. Tjhung, A. Tiribocchi, D. Marenduzzo, and M.E. Cates. A minimal physical model captures the shapes of crawling cells. *Nat. Commun.*, 6:5420, 2015.
 - 48 E. Tjhung, M.E. Cates, and D. Marenduzzo. Nonequilibrium steady states in polar active fluids. *Soft Matter*, 7:7453–7464, 2011.
 - 49 A.N. Beris and B.J. Edwards. *Thermodynamics of Flowing Systems*. Oxford Engineering Science Series. Oxford University Press, 1994.
 - 50 P.G. de Gennes and J. Prost. *The physics of liquid crystals*. The International series of monographs on physics. Oxford University Press, 2nd edition, 1993.
 - 51 S.A. Brazovskii. Phase transition of an isotropic system to a nonuniform state. *J. Exp. Theor. Phys.*, 41:85, 1975.
 - 52 G. Gonnella, E. Orlandini, and J.M. Yeomans. Spinodal decomposition to a lamellar phase: Effects of hydrodynamic flow. *Phys. Rev. Lett.*, 78:1695, 1997.
 - 53 G. Pätzold and K. Dawson. Connection of microstructure to rheology in a microemulsion model. *Phys. Rev. E*, 54:1669–1682, Aug 1996.
 - 54 G. Pätzold and K. Dawson. Rheology of self-assembled fluids. *J. Chem. Phys.*, 104(15):5932–5941, 1996.
 - 55 G. Gompper, C. Domb, M. S. Green, M. Schick, and J. L. Lebowitz. *Phase Transitions and Critical Phenomena: Self-assembling amphiphilic systems*. Phase transitions and critical phenomena. Academic Press, 1994.
 - 56 G. Gompper and M. Kraus. Ginzburg-landau theory of ternary amphiphilic systems. i. gaussian interface fluctuations. *Phys. Rev. E*, 47:4289–4300, Jun 1993.
 - 57 S.J. Jaju and V. Kumaran. Structure-rheology relationship in a sheared lamellar fluid. *Phys. Rev. E*, 93:032609, 2016.
 - 58 L. Carenza, G. Gonnella, A. Lamura, G. Negro, and A. Tiribocchi. *arXiv:1906.01129, in production on epje*, 2019.
 - 59 C. Denniston, E. Orlandini, and J.M. Yeomans. Lattice boltzmann simulations of liquid crystal hydrodynamics. *Phys. Rev. E*, 63:056702, 2001.
 - 60 W. Gropp, E. Lusk, and A. Skjellum. *Using MPI: Portable Parallel Programming with the Message Passing Interface*. Scientific and Engineering Computation. The MIT Press, 2 edition, 1999.
 - 61 S. Succi. *The Lattice Boltzmann Equation: For Fluid Dynamics and Beyond*. Numerical Mathematics and Scientific Computation. Clarendon Press, 2001.
 - 62 G. Li, J. Besson, L. Nisimova, D. Munger, P. Mahautmr, J.X. Tang, M.R. Maxey, and Y.V. Brun. Accumulation of swimming bacteria near a solid surface. *Phys. Rev. E*, 84:041932, 2011.
 - 63 M.A. Wozniak, K. Modzelewska, L. Kwong, and P.J. Keely. Focal adhesion regulation of cell behavior. *Biochim. Biophys. Acta*, 1692(2):103 – 119, 2004.
 - 64 L. Giomi, M.J. Bowick, P. Mishra, R. Sknepnek, and M.C. Marchetti. Defect dynamics in active nematics. *Philosophical Transactions of the Royal Society of London A: Mathematical, Physical and Engineering Sciences*, 372(2029), 2014.
 - 65 Note that unviscid motion occurs in the model of³⁷ only with symmetric profiles, with shear gradient all localized in the bulk.
 - 66 S.R. de Groot and P. Mazur. *Non-Equilibrium Thermodynamics*. North-Holland and Publishing Company, 1962.
 - 67 K. Kruse, J.F. Joanny, F. Jülicher, J. Prost, and K. Sekimoto. Generic theory of active polar gels: a paradigm for cytoskeletal dynamics. *Eur. Phys. J. E*, 16(1):5–16, 2005.
 - 68 R.C. Dewar, C.H. Lineweaver, R.K. Niven, and K. Regenauer-Lieb. *Beyond the Second Law: Entropy Production and Non-equilibrium Systems*. Understanding Complex Systems. Springer Berlin Heidelberg, 2013.

- 69 F. Schlögl. Chemical reaction models for non-equilibrium phase transitions. *Zeitschrift für Physik*, 253(2):147–161, Apr 1972.
- 70 R.G. Endres. Entropy production selects nonequilibrium states in multistable systems. *Scientific Reports*, 7(6):14437, 2017.
- 71 O. Henrich, K. Stratford, D. Marenduzzo, P.V. Coveney, and M.E. Cates. Rheology of lamellar liquid crystals in two and three dimensions: a simulation study. *Soft Matter*, 8:3817–3831, 2012.
- 72 L.N. Carenza, G. Gonnella, A. Lamura, and G. Negro. Dynamically asymmetric and bicontinuous morphologies in active emulsions. *Int. J. Mod. Phys. C*, 0(0):1941002, 2019.

A Adimensional numbers

In this Appendix we will furnish a derivation for the compression modulus B that we made use of to define the adimensional Ericksen number, Er , and the *active* Ericksen number Er_{act} .

In the following we consider the elastic coefficients for a binary mixture in the lamellar phase, in which one of the components is an isotropic fluid and the other is a polar liquid crystal. One of them, the compression modulus, is used to define the adimensional Ericksen number Er and its active counterpart Er_{act} , in terms of the model parameters. The analytical treatment generalizes that given in⁵⁷ for a simple lamellar fluid.

It is first convenient to rewrite the Landau-Brazovskii free-energy functional of Eq. (9) in a more symmetric form, in terms of the field $\psi = \phi - \phi_{cr}$, as

$$F[\psi, \mathbf{P}] = \int d\mathbf{r} \left[\frac{\tilde{a}}{2} \psi^2 + \frac{b}{2} \psi^4 + \frac{k_\phi}{2} |\nabla \psi|^2 + \frac{c}{2} (\nabla^2 \psi)^2 - \frac{\alpha}{2} \psi |\mathbf{P}|^2 + \frac{\alpha}{4} |\mathbf{P}|^4 + \frac{k_P}{2} (\nabla \mathbf{P})^2 + \beta \mathbf{P} \cdot \nabla \psi \right]. \quad (28)$$

Eq. (9) of the main text can be obtained with $\tilde{a} = -a/\phi_{cr}^2$, $b = a/\phi_{cr}^4$ and $\phi_0 = 2\phi_{cr}$. At equilibrium, the chemical potential μ and the molecular field \mathbf{h} must vanish:

$$\mu \equiv \frac{\delta F}{\delta \psi} = \tilde{a} \psi + b \psi^3 - k_\phi \nabla^2 \psi + c \nabla^4 \psi - \alpha \mathbf{P} - \beta \nabla \cdot \mathbf{P} = 0, \quad (29)$$

$$\mathbf{h} \equiv \frac{\delta \mathbf{F}}{\delta \mathbf{P}} = -\alpha \psi \mathbf{P} + \alpha \mathbf{P}^2 \mathbf{P} - k_P \nabla^2 \mathbf{P} + \beta \nabla \psi = 0. \quad (30)$$

We then take the single mode approximation⁵⁷, exact if considering only gradient terms in the above expressions,

$$\psi = \tilde{\psi} \sin(\kappa y), \quad (31)$$

where the amplitude $\tilde{\psi}$ and the wavenumber κ of the modulation have to be computed. Our simulations confirm that, as long as bulk parameters are small if compared to the elastic ones, the concentration field is modulated in a sinusoidal fashion. By substituting Eq. (31) into Eq. (30), and neglecting non linear contributions, we find that P_y must satisfy,

$$\partial_y^2 P_y = -\frac{\beta \kappa}{k_P} \tilde{\psi} \sin(\kappa y), \quad (32)$$

whose periodic solutions, with lamellar width $\lambda = 2\pi/\kappa$, are given by

$$P_y = C + \frac{\tilde{P}}{\kappa} \cos(\kappa y), \quad (33)$$

where C is a constant and

$$\tilde{P} = \beta \tilde{\psi} / k_P. \quad (34)$$

In order to find the coefficients C , $\tilde{\psi}$ and the wavenumber κ , we substitute profiles of ψ and P_y in Eq. (28), integrate over the lamellar wavelength λ and minimize with respect to κ , that is found to be $\sqrt{|k_\phi|/2c}$, the same as for the polarization-free case. Thus we rewrite the free-energy density as

$$f = \frac{1}{4} \left[(\tilde{a} - a_\phi - a_P) \tilde{\psi}^2 + \frac{3}{8} \left(b + \frac{4\alpha c^2 \beta^4}{k_\phi^2 k_P^4} \right) \tilde{\psi}^4 + \alpha C^2 \left(C^2 - \frac{6c\beta^2 \tilde{\psi}^2}{k_\phi k_P^2} \right) \right], \quad (35)$$

where we defined $a_\phi = k_\phi^2/4c$ and $a_P = \beta^2/k_P$. Minimization of f with respect to C gives $C = 0$. Then, by further minimizing f with respect to $\tilde{\psi}$, we find

$$\tilde{\psi} = \pm 2|k_\phi| k_P^2 \sqrt{\frac{a_\phi + a_P - \tilde{a}}{3(k_\phi^2 k_P^4 b + 4\alpha c^2 \beta^4)}}. \quad (36)$$

This result shows that lamellar ordering occurs for $\tilde{a} < a_{cr} = a_\phi + a_P$. Thus, polarization enlarges the range of stability of the lamellar phase with respect to the Brazovskii theory, where lamellar ordering occurs if $\tilde{a} < a_\phi$.

We now introduce the elastic coefficients related to the free-energy cost of deviations from the harmonically modulated profile. We perturb equilibrium profiles by introducing a layer perturbation field $\vartheta(x, y)$, in terms of which the perturbed profiles become

$$\psi(x, y) = \tilde{\psi} \sin[\kappa(y - \vartheta(x, y))], \quad (37)$$

$$P(x, y) = \frac{\tilde{P}}{\kappa} \cos[\kappa(y - \vartheta(x, y))]. \quad (38)$$

The field ϑ is chosen so that its amplitude is much smaller than the lamellar width λ , but its typical variation lengthscale is much wider.

Because of the slowly-varying behaviour of ϑ , we flush out high-frequency modes to obtain a coarse-grained description of the model solely in terms of the layer displacement. This implies⁵⁷ that the following normalization condition holds:

$$\left[\frac{1}{L_x L_y} \int d\mathbf{r} \sin^2[\kappa(y - \vartheta(x, y))] \right]_{cg} = 1, \quad (39)$$

where L_x and L_y are the linear dimensions of the system and the boundary conditions are assumed to be periodic in both directions. By substituting Eqs. (37)-(38) and their derivatives in Eq. (28) and by retaining only the elastic contributions, namely the gradient terms, we find the following coarse-grained free-

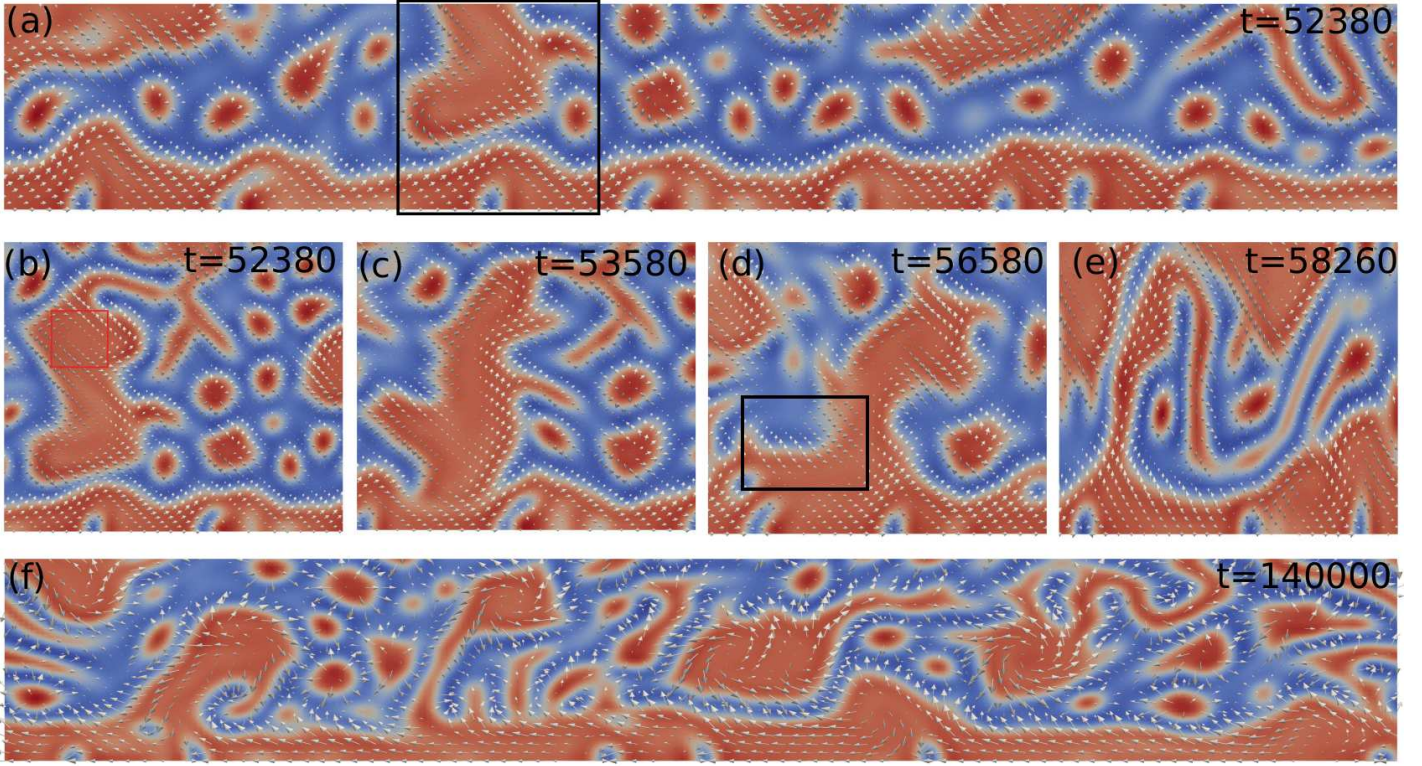


Fig. 9 Polarization flip. Contour plots of concentration field ϕ for $\zeta = 0.005$ ($Er_{act} = 0.57$) and $\dot{\gamma} = 3.12 \times 10^{-5}$ ($Er = 0.003$). Panels (a) and (f) show the initial and final state, respectively, of the polarization at the bottom wall. Panels (b-e) show snapshots of the collision of a droplet with the bottom wall, which causes a local rearrangement of the polarization state. The red contour in panel (b) encloses a +1 defect in the polarization field pattern.

energy functional:

$$\begin{aligned}
 F_{cg}[\vartheta] &= \int d\mathbf{r} \frac{\tilde{\Psi}^2}{2} \left[\left(k_\phi \kappa^2 + 2c\kappa^4 + \frac{\beta^2}{k_p} \right) (\partial_x \vartheta)^2 \right. \\
 &\quad \left. + \left(k_\phi \kappa^2 + 6c\kappa^4 + \frac{\beta^2}{k_p} \right) (\partial_y \vartheta)^2 + c\kappa^2 (\nabla^2 \vartheta)^2 \right] \\
 &\equiv \int d\mathbf{r} \left[\frac{\Sigma}{2} (\partial_x \vartheta)^2 + \frac{B}{2} (\partial_y \vartheta)^2 + \frac{\Upsilon}{2} (\nabla^2 \vartheta)^2 \right] \quad (40)
 \end{aligned}$$

where we have used Eq. (39), and Eq. (34) to get rid of \tilde{P} . In this expression we identify three contributions, combination of the three following effects: (i) stretching/shrinking of the lamellar surface in the layer direction (x in this Section), (ii) compression/expansion of the lamellar layers in the gradient direction (y) and (iii) bending of the layers.

The coefficient of the derivative along the gradient direction is half of the compression modulus B and it gives the energy penalty per unit surface due to a change in the layer width. Its explicit expression is then given by

$$B = \left(\frac{\beta^2}{k_p} + \frac{k_\phi^2}{c} \right) \tilde{\Psi}^2. \quad (41)$$

Analogously we can define the surface tension Σ as the energy penalty per unit surface due to the stretching of the layer as half

of the coefficient in the layer direction

$$\Sigma = \left(\frac{\beta^2}{k_p} - \frac{k_\phi^2}{2c} \right) \tilde{\Psi}^2. \quad (42)$$

It is worth noticing that, from one side, the liquid crystal network makes the lamellar structure stiffer, since the compression modulus is strengthened with respect to the polarization-free model, while on the other side, it counterbalances the negative surface tension of the lamellar phase. *In ultimis*, the coefficient of the laplacian term is half of the curvature modulus, which gives the energetic cost associated to an infinitesimal bending of a layer. It can be written as

$$\Upsilon = \frac{k_\phi}{2} \tilde{\Psi}^2. \quad (43)$$

B Polarization flip

In this Section we illustrate the mechanism at the origin of the flip of polarization at the boundary, giving rise to intermittent viscosity behaviour, characterizing the blue region of the phase diagram presented in Fig. 8. This phenomenon is driven by the collision of active domains against the boundary layers. In Fig. 9 we show, for the case at $Er_{act} = 0.57$, $Er = 0.003$, a series of snapshots of a change of polarization on the bottom wall from the antiparallel alignment of \mathbf{P} with respect to the imposed velocity ($-$ state) to a parallel configuration ($+$ state). The overall dynamics of the event can be better appreciated by looking at the attached Movie 3,4. Panel (a) of Fig. 9 shows the configuration at time $t = 52380$, before the event. Panel (b) shows a zoom at the same time of a colliding active domain, characterized by a typical

vortical pattern in the polarization field, with a +1 defect, highlighted by a red square in panel (b). As the droplet merges with the layer, strong elastic interactions produce bendings of the liquid crystal network (see panel (c) at time $t = 53580$). In panel (d) at a close subsequent time $t = 56580$, the system is still found in a homogeneous $-P_w$ state on the wall, despite the polarization on the top part of the layer is now directed in the same direction of the imposed flow. The +1 defect has disappeared due to the interaction with the wall, thus generating a complex rearrangement dynamics. As a result of the advection and the elastic deforma-

tions, the polarization flap, directed along the flow direction and highlighted by the black box in panel (d), is pushed on the walls and adheres on it, resulting in a local change of the polarization state (see panel (e) at time $t = 58286$). After a similar event, not shown in Fig. 9, the overall hydrodynamic state changes, thus leading to a final homogeneous + state, shown in panel (f). We observe that flip dynamics generally takes place on time-scale of order $\sim \mathcal{O}(10^5)$ timesteps, much shorter than the lifetime of viscosity states that are found to be $\sim \mathcal{O}(10^7)$.